Characterization of artificial structural anomalies in a graphite test article via in-situ vibration monitoring and machine learning

Paul Geimer, Andrew Delorey, and Anna Patelli

LA-UR-26-28283
September 18, 2026

Los Alamos
NATIONAL LABORATORY

Prepared by: Paul Geimer, Scientist
Structure / Property Relations (MST-8)
Los Alamos National Laboratory

Prepared for: U.S. Department of Energy
Office of Nuclear Energy
John H. Jackson, National Technical Director, DOE-NE Microreactor Program



NOTICE: This report was prepared as an account of work sponsored by an agency of the United States Government. Neither the United States Government, nor any agency thereof, nor any of their employees, nor any of their contractors, subcontractors, or their employees, make any warranty, express or implied, or assume any legal liability or responsibility for the accuracy, completeness, or usefulness of any information, apparatus, product, or process disclosed, or represent that its use would not infringe privately owned rights. Reference herein to any specific commercial product, process, or service by trade name, trademark, manufacturer, or otherwise, does not necessarily constitute or imply its endorsement, recommendation, or favoring by the United States Government, any agency thereof, or any of their contractors or subcontractors. The views and opinions expressed herein do not necessarily state or reflect those of the United States Government or any agency thereof.

Acknowledgments

This work is supported by the Microreactor Program of the US Department of Energy's Office of Nuclear Energy. Damien Milazzo provided prototype designs and fabrication assistance for insertable plugs. Erik Luther, Holly Trellue, and Tarik Saleh assisted in acquiring a relevant graphite component for testing. Generative AI tools were used in a limited, supportive capacity during the preparation of this document for editing, structure, and formatting assistance. The authors have reviewed and take full responsibility for all content herein.



NOTICE: This report was prepared as an account of work sponsored by an agency of the United States Government. Neither the United States Government, nor any agency thereof, nor any of their employees, nor any of their contractors, subcontractors, or their employees, make any warranty, express or implied, or assume any legal liability or responsibility for the accuracy, completeness, or usefulness of any information, apparatus, product, or process disclosed, or represent that its use would not infringe privately owned rights. Reference herein to any specific commercial product, process, or service by trade name, trademark, manufacturer, or otherwise, does not necessarily constitute or imply its endorsement, recommendation, or favoring by the United States Government, any agency thereof, or any of their contractors or subcontractors. The views and opinions expressed herein do not necessarily state or reflect those of the United States Government or any agency thereof.

Contents

Acronyms and Abbreviations v
Executive Summary vi
1 Introduction 1
2 Scope of Work 2
3 Methodology 3
3.1 Sample and Hardware Descriptions 3
3.2 Experimental Setup 4
3.3 Machine Learning Approach 7
3.3.1 Model Architecture and Data Representation 7
3.3.2 Software for Data Processing 8
4 Results and Discussion 9
5 Conclusions and Future Work 12
6 References 14

Figures

Figure 1. Removable expanding plugs considered for generating reversible, localized stress anomalies within the graphite component. (top) Rubber plug used in previous testing. (middle two) Prototype double-action plugs made from 3D-printed carbon-fiber-reinforced filament. (bottom) Modified expanding steel mandrel used for experimental testing in this report. 4
Figure 2. Schematic of experimental setup, showing virtual sensor locations and minimum and maximum insertion depths tested for the expanding mandrel. 5
Figure 3. Comparison of two data sets measured at different virtual sensors and for different mandrel locations. From top to bottom: raw time series (shown as voltage amplitude, proportional to velocity), spectrogram, and amplitude spectrum. (left column) Data from virtual sensor 0 with mandrel at 0 cm. (right column) data from virtual sensor 11 with mandrel at 14 cm. While the raw time series is expectedly noisy in both, due to the nature of the excitation source, the amplitude spectra show distinct differences in spectral peak amplitudes and locations due to the spatially varying patterns of resonance across the component. 6
Figure 4. Architecture of GNN-FNO model used in this study [26]. 7
Figure 5. (left) Flowchart of user interface for both training and prediction workflows. (right) Screenshots of interface inputs and outputs during model training (top) and generation of predictions (bottom). 8
Figure 6. Predictions of the experimental configuration for an expanding mandrel in three configurations: absent, and inserted into the graphite block in a low-stress configuration at two locations (0 and 14 cm). Correct predictions in these confusions matrices fall along the diagonal. 10
Figure 7. Predictions of the experimental configuration for an expanding mandrel in five configurations: absent, and inserted into the graphite block in a low-stress and high-stress configuration at two locations (0 and 14 cm). 11
Figure 8. Location predictions for an expanding mandrel inserted into the graphite block in a low-stress configuration at 15 depths, from 0 to 14 cm. Each column/row represents a 1-cm increment in the location of the inserted mandrel. 12

ACRONYMS AND ABBREVIATIONS

Acronym	Definition
CLI	command-line interface
DAQ	data acquisition system
DOE-NE	Department of Energy, Office of Nuclear Energy
FFT	fast Fourier transform
FNO	Fourier neural operator
GNN	graph neural network
LANL	Los Alamos National Laboratory
LDV	laser Doppler vibrometer
ML	machine learning
MRP	Microreactor Program
NDE	non-destructive evaluation
SHM	structural health monitoring

EXECUTIVE SUMMARY

Nuclear microreactors offer adaptable, portable, and cost-effective clean energy for remote sites, industry, and microgrid use. Their compact size and efficient construction require advanced automation, minimal staffing, and long operation periods with limited maintenance, making reliable structural health monitoring crucial for detecting early deterioration in reactor components. While graphite is commonly used for neutron moderation and structural roles, its quasi-brittle nature, sensitivity to radiation, and shifting internal stresses make continuous monitoring challenging. Conventional nondestructive evaluation methods are difficult to use consistently in these compact, high-temperature, and high-radiation environments, highlighting the need for improved diagnostic approaches.

This report outlines technical progress since March 2026 by the LANL Instrumentation and Sensors team on expanding non-destructive inspection of graphite components through machine-learning-based vibration analyses, supporting DOE-NE Microreactor Program (MRP) goals. Early in the fiscal year, progress towards technology maturation was demonstrated with the limited machine learning predictions about the status of a localized, reversible stressor in a hexagonal graphite block. However, later analysis indicated that variable noise in input data may have biased machine learning performance and that local stresses were likely insufficient for consistent characterization. Therefore, results reported here are based on a modified stress source and updated data acquisition procedures.

In this work, we have applied this modified stressor to demonstrate further generalizability of our machine-learning-based method for structural health monitoring in graphite components with geometries relevant to nuclear microreactors. Testing under steady-state conditions where the vibrational and environmental conditions remained consistent, we find that coarse locating of an inserted metal plug is successfully achieved at rates of 80-90% with a hybrid graph neural network, even under differing stress levels. Successful predictions of fine-scale localization with 1 cm accuracy were achieved at rates four times greater than random chance, demonstrating sensitivity to subtle location changes. Towards further technology maturation, back-end development has produced a new command-line interface that helps to streamline and standardize data processing, training and validation of machine learning models, and generation of classification predictions from test data as well as summary figures of model performance.

While results contained within this report are specifically tied to surface vibration measurements, the methods described are not reliant on a specific type of data or sensor, and numerous types of continuous sensing data could be substituted or combined to provide enhanced structural health monitoring. For example, approaches such as ultrasonic, acoustic emission, thermal, or electrical measurements could be integrated alongside vibration data, either individually or in combination, to capture a broader range of material responses and improve the reliability and sensitivity of in situ defect detection and condition assessment in graphite components.

To provide a self-contained account of the work, we note that portions of the technical background, methodology, and selected figures are reproduced or adapted from previous project reports. The relevant reports are cited where applicable.

1 Introduction

Compared to conventional gigawatt-scale nuclear reactors, microreactors offer several advantages: ease of transport, enhanced passive safety, minimal operational footprint, and factory fabrication. However, their reduced power output (typically <20 MWe) limits economies of scale, making low maintenance and operational costs essential for commercial viability outside niche applications such as rural communities, disaster relief, or remote military installations. Private industry and the US Department of Energy are pursuing increased automation of reactor operations to reduce staffing costs – a goal that enhanced monitoring techniques can directly support.

Structural health monitoring (SHM) is a particular concern for microreactors, which are designed to operate in more extreme environments than conventional reactors while minimizing inspection and refueling, procedures that decades of commercial nuclear experience have refined into established best practices from both business and safety standpoints. Minimizing these procedures shifts greater burden onto reactor components to perform continuously and reliably under harsh conditions, often exceeding prior testing envelopes, while compact reactor assemblies simultaneously restrict physical access for inspection.

This challenge is especially acute for graphite, a foundational core material in reactor design since the earliest moderated reactors due to its low neutron absorption cross section and high thermal stability [1]. Graphite remains essential to high-temperature gas-cooled reactors, molten-salt concepts, and an increasing number of heat-pipe microreactor designs [2]. Despite these favorable properties, graphite is a complex, quasi-brittle material with a hierarchical microstructure that degrades non-linearly under irradiation and temperature. Dose- and temperature-dependent dimensional change, irradiation creep, and degradation of elastic, thermal, and electrical properties arise from defect accumulation, pore evolution, and crystallographic anisotropy [3–5]. Microcracks nucleate at pores and stress concentrations before propagating and coalescing across multiple length scales [1,6,7]. Recent experimental and modeling work has substantially advanced understanding of graphite strength, damage tolerance, and lifetime prediction, supporting safety cases for current and next-generation graphite-moderated reactors [8–11]. Collectively, this body of work shows that even small changes in internal stress state or pore morphology can produce measurable shifts in material properties or dynamic behavior—changes that, ideally, would be monitored in situ to enable early shutdown or component replacement before failure.

Conventional non-destructive evaluation (NDE) techniques—X-ray computed tomography, ultrasonic methods, eddy-current inspection, and neutron imaging—provide valuable structural insight but are poorly suited to in situ deployment in microreactors, where small form factors, high temperatures, and intense radiation fields restrict sensor and human access, and many methods require line-of-sight, coupling media, or physical contact incompatible with compact containment designs.

Vibration-based SHM offers a promising alternative: resonance frequencies, mode shapes, and broadband spectral content are inherently sensitive to changes in stiffness, density distribution, microcracking, and boundary conditions, and have previously been used to identify damage in

conventional reactor components via shifts in dynamic signatures [12,13]. Recent demonstrations of optical-fiber-based vibration sensing at temperatures approaching 800°C [14–16], suggest feasibility for microreactor environments specifically. The remaining challenge is interpreting defect signals in vibration data reliably and autonomously without relying on operator expertise.

Machine learning (ML) offers one potential solution. Traditional reactor SHM remains largely manual or schedule-driven, leaving room for data-driven approaches to improve sensitivity and efficiency [17]. Modern ML methods excel at extracting multidimensional patterns from broadband vibration data without requiring fully specified physics models [18,19], and have been applied successfully to SHM and NDE in metallic structures [20,21]. While graphite's high porosity and internal damping can dampen signal sharpness relative to metals, this has not precluded successful defect detection in surrogate graphite fuel elements [22]. Among ML architectures, neural networks—particularly graph neural networks (GNNs), which suit spatially distributed sensor configurations—have proven broadly effective. Fourier neural operators (FNOs) have more recently emerged as a powerful framework for learning operator mappings in PDE-governed systems, including wave propagation and elastic deformation, with demonstrated generalization and computational efficiency across diverse physical systems [23–25].

Prior MRP-funded work demonstrated initial feasibility for detecting internal stress anomalies in graphite using vibration measurements, but was limited by inconsistent stress application, poor repeatability, and coarse spatial resolution [26]. This project builds directly on those results, combining laser Doppler vibrometer (LDV) measurements of surface vibrations with a hybrid neural-operator ML framework to learn defect-sensitive vibrational signatures from broadband surface response data. The approach is demonstrated on a hexagonal graphite block containing internal channels—representative of graphite core geometries in candidate microreactor designs—to evaluate whether small, localized internal stress anomalies can be reliably detected and localized using surface-only measurements. This work establishes a foundation for autonomous, minimally intrusive SHM suited to the access constraints and extended operational demands of microreactor systems.

2 Scope of Work

The primary goal of this work is to demonstrate localization sensitivity to a small stress anomaly within a representative graphite component using surface vibration data. A neural-operator-enhanced ML framework will be used to parse the resulting waveforms and identify defect-sensitive features. A secondary goal is to refine the processing workflow so predictions can be generated and interpreted without specialized expertise in vibration analysis or ML.
This effort builds on prior MRP-funded work, which demonstrated initial feasibility but was limited by inconsistent stress application and coarse spatial resolution. The tasks below were chosen to address those limitations.

1. **Coarse defect localization.** Using an improved experimental setup with better control over stress amplitude, this task will demonstrate coarse-level localization of an internal stress anomaly within a hexagonal graphite block containing internal channels, using LDV-collected surface vibration data processed through the hybrid ML model. The

targeted outcome is correct identification of the general region containing the induced anomaly, benchmarked against prior MRP-focused results.

2. **Sensitivity testing.** This task will assess the sensitivity of the predictive model to the precise characteristics of the induced stress anomaly, establishing minimum thresholds for location and stress levels. The targeted outcomes are quantified limits for the specific experimental design tested in this study, and qualitative guidance for more general uses.

3. **Workflow refinement.** The processing and deployment workflow will be streamlined to minimize manual tuning, enabling consistent use by non-specialist personnel. The targeted outcome is a documented, repeatable pipeline suitable for producing consistent predictions across operators/trials without retraining.

Future work: Testing this approach on a confirmed failing component using multi-modal data representative of those present in microreactor control systems has been identified as a potential high-value follow-on goal that was out-of-scope for this year's efforts.

3 Methodology

3.1 Sample and Hardware Descriptions

The sample tested and characterized in this study is the same as that tested in recent MRP-supported efforts: a hexagonal graphite monolith containing 19 uniformly spaced axial channels (bores) with diameters of 15.1 ± 0.2 mm. The 10 cm wide by 30 cm long sample (herein referred to as the "component") is comparable to those used in recent test bed experiments [27–29], but is not associated with any specific reactor design, vendor, or classified/controlled configuration. The component is made from isostatically molded graphite (grade 2124 from Mersen) with high strength, fine grain (mean grain size of 13 μm) and isotropic properties comparable to the graphite used in past and present reactors [1,30]. A bare 2 mm thick x 12.7-mm diameter piezoelectric transducer was bonded using super glue to the long face of the component near one end to ensure consistent excitation conditions, resulting in a total mass of 1943.6 g for the component-transducer system.

The structural anomaly used for testing was applied in the form of an insertable expanding plug that can be locked into place at a known location and stress level to apply a repeatable, but removable and non-damaging stress anomaly. The notable change made from past experimental testing was reengineering the insertable plug that previously provided the localized stress anomaly within the graphite core block [26] (Figure 1). Recent data analysis suggested that an expanding plug made of rubber used in previous testing did not generate sufficient structural stress to cause detectable changes in the ambient vibrational wavefield, resulting in inconclusive ML predictions about the status and location of the plug. Initial prototyping focused on 3D printed designs using carbon-fiber-reinforced filament and a double-action expansion mechanism that could be actuated from outside the component to drive four concave plates outwards into the graphite. However, this was found to have repeatability issues during testing that made it challenging to collect independent, but self-similar datasets for use in training and inference (prediction) phases of ML model development. In testing performed for this report, limitations of

prior plug designs were addressed by moving to a stronger steel mandrel customized for the component geometry.



Figure 1. Removable expanding plugs considered for generating reversible, localized stress anomalies within the graphite component. (top) Rubber plug used in previous testing. (middle two) Prototype double-action plugs made from 3D-printed carbon-fiber-reinforced filament. (bottom) Modified expanding steel mandrel used for experimental testing in this report.

Due to the unique requirements for the mandrel in this testing (capable of insertion, tightening, and removal at least 14 cm down the narrow opening of the bore), we modified an off-the-shelf expanding mandrel (Dunham Tool Expanding Mandrel #MMX). Compared to other commercial offerings, this particular model is simple and compact, using a tapered draw bolt to uniformly drive apart the three wedges of a 28.7 mm-long (1.13") slotted steel sleeve, which then expands to grip the graphite from the inside. Expanding mandrels have a narrow working range due to the elastic limits of steel (given as 0.005-0.008" for this model). For this reason, we machined and sanded the original 15.86 mm (5/8") diameter sleeve down to a slip fit, where the sample was just narrow enough to move without hindrance instead the bore. The 9.53 mm (3/8") diameter shank of the mandrel – typically held in the lathe chuck during conventional machining use cases – was machined into a 5/16" hex to enable a socket wrench to prevent the mandrel from freely rotating as the draw bolt was tightened from the other end. After machining, the mass of the mandrel was measured to be 45.5 g, or 2.3% that of the component-transducer system.

3.2 Experimental Setup

Excitation and measurement techniques used for experimentation were largely unchanged from those used in past testing (e.g. [26,31]), with an arbitrary waveform generator (NI PXIe-5413) controlled by a LabVIEW interface supplying a repeatable white-noise input waveform. The resulting signal voltage was externally amplified by a factor of 20 (TEGAM model 2350) before reaching the adhered transducer (Figure 2). White-noise excitation was selected to simulate a passive monitoring environment, where broadband vibrations from operational or ambient sources would be used for excitation. For maximum experimental flexibility and adaptability, surface vibrations were measured via a non-contact single-point LDV operating in the short-wavelength infrared (Polytec VibroFlex QTec). The analog voltage output time series was digitized via a NI PXIe-5122 scope card. 10-second measurements were made at 200 kHz in a 1D line across the sample, with 12 points spaced at 1" increments. The LDV remained in one location during all testing, with the component manually translated in front of the laser spot at a fixed distance (beam length was about 5 cm). This excitation-measurement configuration

simulates a sensor array in which all 12 locations ("virtual sensors") were measuring simultaneously.

Past experiments on the graphite component suffered from systematic differences in noise floor of the LDV measurements that, while only discernable when viewing spectral amplitudes in a logarithmic decibel scale – likely biased the model towards accurate predictions, as the model could learn the noise floor associated with each test at a virtual sensor location, rather than the intended spectral details associated with the resonance peaks. The likely source of this noise was small changes in the LDV focus as the component was repositioned between each test. This was addressed by locking the laser focus and carefully maintaining a fixed distance from the LDV to the surface of the sample.

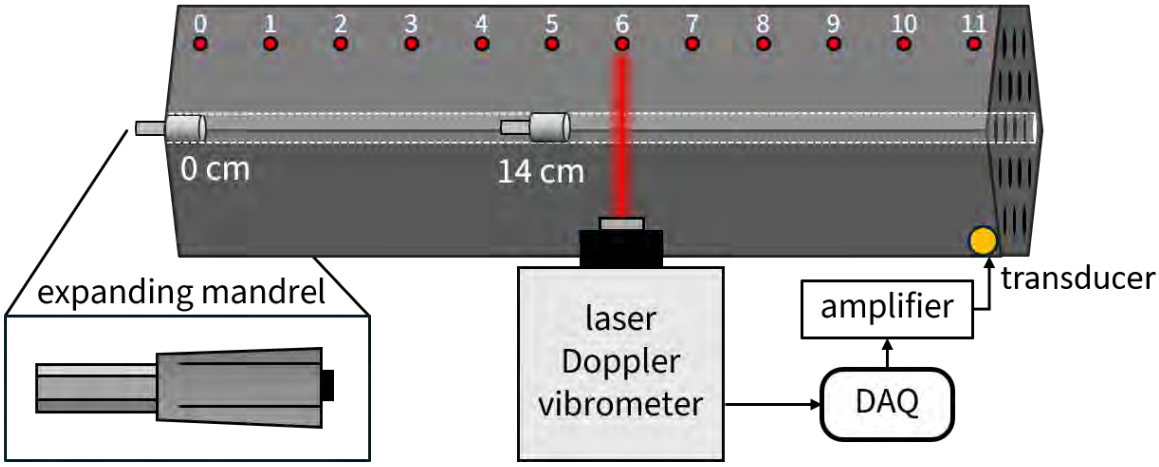


Figure 2. Schematic of experimental setup, showing virtual sensor locations and minimum and maximum insertion depths tested for the expanding mandrel.

The two variables modified during testing were the insertion depth of the mandrel and the stress applied by the mandrel to the component. Each dataset was collected using the same bore in the component to improve experimental repeatability. Insertion depth was measured from the bottom of the sleeve, where a depth of 0 cm indicates the bottom of the sleeve was flush with the end face of the component and the leading edge of the mandrel was 28.7 mm into the bore. Depths of up to 14 cm were tested, which roughly positioned the mandrel at the lengthwise midpoint of the component. Greater depths were not tested since the component is symmetric along its length. When the mandrel was inserted into the component, two levels of applied stress were tested. The "low-stress" configuration was defined as the mandrel being slightly expanded, fine-tuning the diameter to create an interference fit where it could be manually repositioned while remaining in contact with the inner walls of the bore. In a "high-stress" configuration, the mandrel can be further expanded to lock in place within the bore. Data collected from this configuration has not yet been fully analyzed but is planned to be combined with depth changes to provide a more complex multi-dimensional test matrix to help validate and constrain model performance. We note that since the mandrel sleeve expands asymmetrically from one end, the contact area likely changes by a small amount between the low- and high-stress configurations. While not quantified directly during testing, this would result in greater stress localization in the high-stress setup.

Repeatability of the configuration was tested by repeatedly removing and repositioning the mandrel at a low-stress level, ensuring that cross-correlation coefficients of measured vibrational spectra between repeated trials were larger than those observed when the experimental configuration changed (different virtual sensor or mandrel depth). A quantitative comparison of the typical variation between measurements made for different configurations can be seen in Figure 3, highlighting the spectral complexity generated by the resonating component under broadband excitation and the utility of ML to efficiently interpret differences in spectral signals.

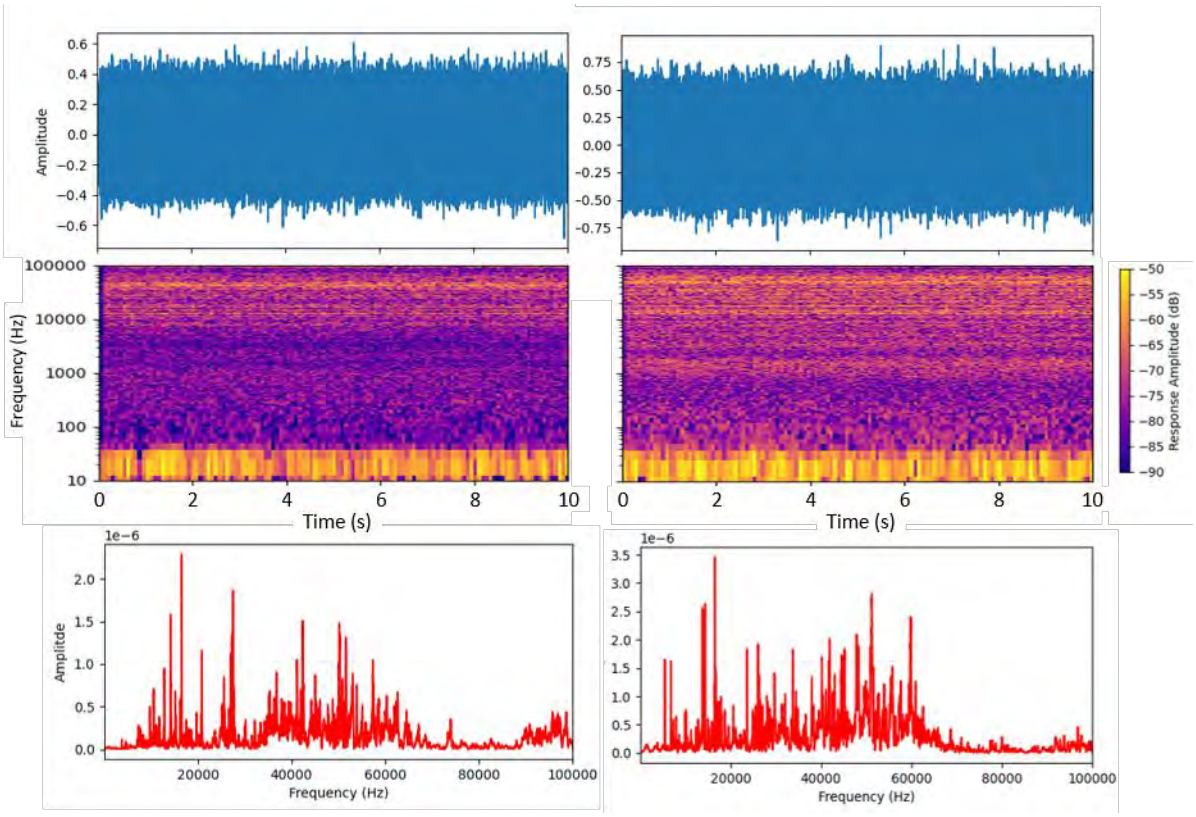


Figure 3. Comparison of two data sets measured at different virtual sensors and for different mandrel locations. From top to bottom: raw time series (shown as voltage amplitude, proportional to velocity), spectrogram, and amplitude spectrum. (left column) Data from virtual sensor 0 with mandrel at 0 cm. (right column) data from virtual sensor 11 with mandrel at 14 cm. While the raw time series is expectedly noisy in both, due to the nature of the excitation source, the amplitude spectra show distinct differences in spectral peak amplitudes and locations due to the spatially varying patterns of resonance across the component.

3.3 Machine Learning Approach

3.3.1 *Model Architecture and Data Representation*

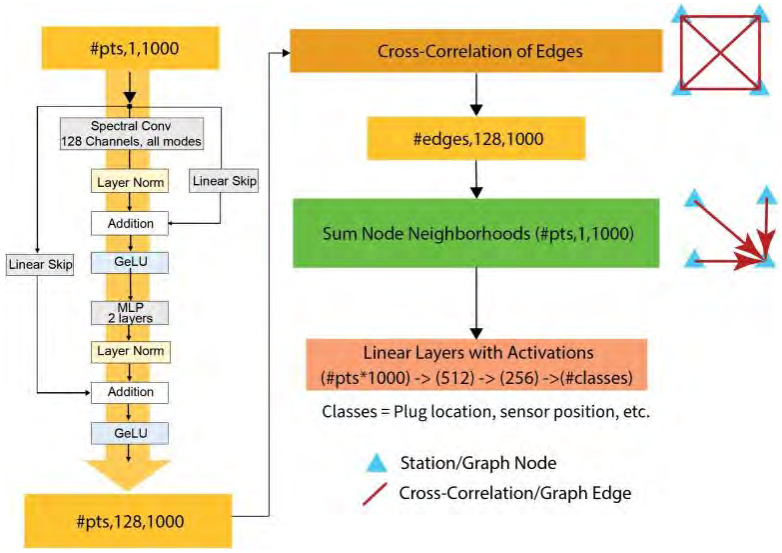


Figure 4. Architecture of GNN-FNO model used in this study [26].

The FNO-GNN model receives an input tensor structured according to the number of measurement nodes and the time-series length recorded at each node. Rather than using the raw time-domain data, each 10-s time series is broken up into sub-windows with lengths of 1000 points (5 ms duration) prior to being input into the network and used for training, validation, or inference. In the first step, the time domain data is converted to the frequency domain using expanded dimensionality and spectral convolutions. This highly granular spectral transformation is important as the frequency domain representations offers a clearer view of the elastic and structural characteristics that are key to the defect classification tasks. In this approach, measurement nodes are treated as vertices in a graph. The edges of this graph are designed to encode how elastic waves propagate between measurement locations and capture spatial variations in standing wave amplitudes within the structure. The hybrid FNO-GNN architecture processes this spectral graph representation, generating node-level embeddings that are then pooled to produce a single, component-scale embedding of the sample. This final pooled embedding is mapped to a predicted elastic state, which supports a range of classification tasks including mandrel presence or absence, mandrel location/depth, or sample identity if comparing larger populations.

All of our current models are category classifications. For some classifications, such as the location of a stress anomaly, we are moving towards increasing numbers of classes with the goal of transitioning to predicting a floating-point value representing the exact location of the anomaly. Since training data has a finite number of examples with a finite number of anomaly locations, this would demonstrate the generalizability of the model. Although some models can train successfully using only one node, we maintain graph architecture for flexibility in adding any number of arbitrary data streams. The only requirement is that the data streams are recorded contemporarily.

3.3.2 *Software for Data Processing*

A dedicated command-line interface (CLI) tool was recently developed to standardize and streamline the data processing and model-training workflow. The tool provides a menu-driven interface that guides the user through data ingestion, model training, prediction, and evaluation, thereby reducing manual overhead and improving reproducibility relative to prior ad hoc scripting approaches. Data can be supplied flexibly, either as a single file or as an entire directory of files, and at present, the tool supports multiple prediction targets relevant to current and past MRP scope, including torque level, stress state, component identification, mandrel expansion level, and other sample properties (Figure 5). Future development will include the ability to scan a data set and compile a list of meta data that can be used for predictions and the ability to train on compound labels, such as combinations of plug locations and torque values applied to the plug.

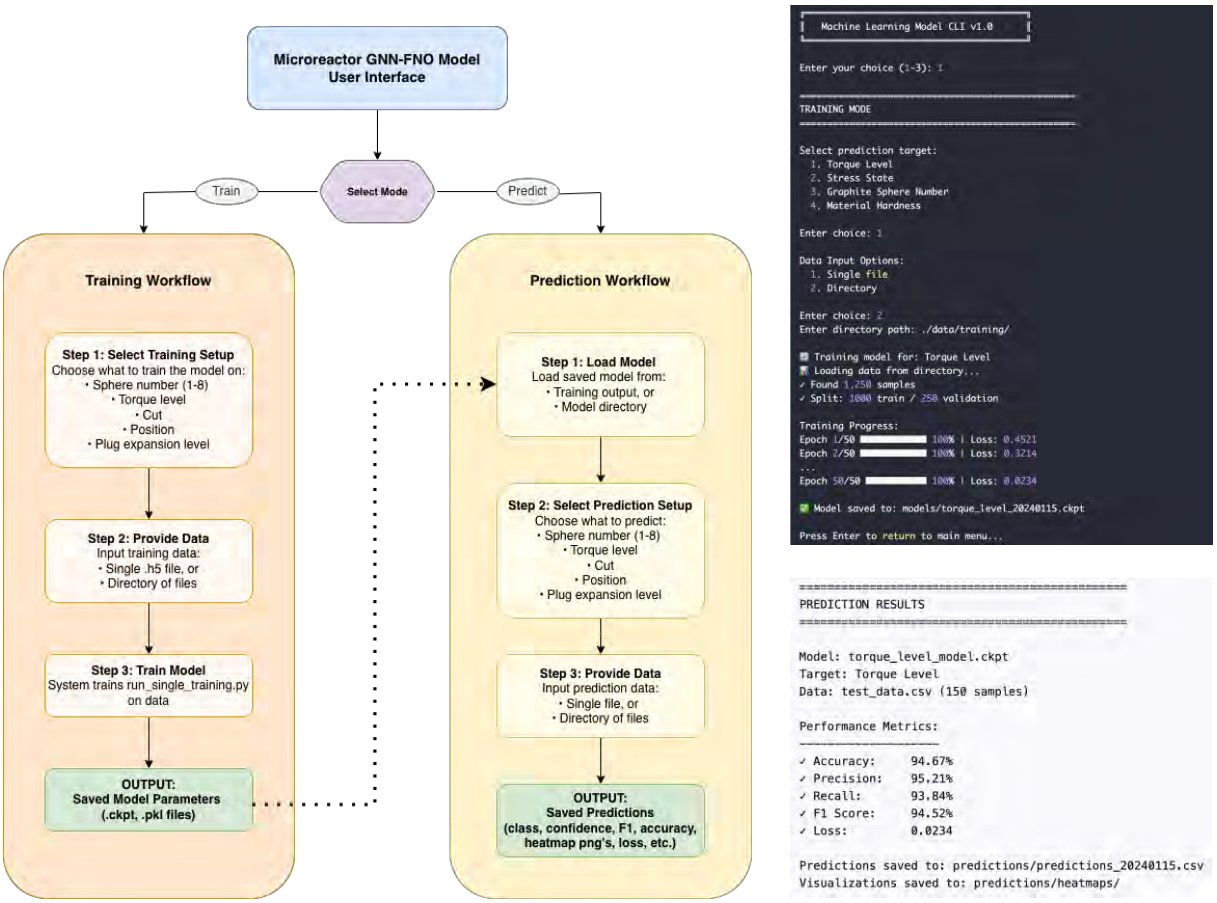


Figure 5. (left) Flowchart of user interface for both training and prediction workflows. (right) Screenshots of interface inputs and outputs during model training (top) and generation of predictions (bottom).

Before training, the user selects the data set to be used and the property that the model should predict; the resulting model parameters are then saved in standard formats (`.pkl` or `.ckpt`) for later reuse. During prediction, the user loads either the most recently trained model or a previously saved model from a specified path, confirms that the prediction target matches the one used during training, and supplies new data in the same file or directory format. The tool

then generates a range of outputs to support evaluation, including predicted classes, confidence scores, F1 score, loss values, and confusion matrix heatmaps. By consolidating these steps into a single guided workflow, the CLI tool standardizes what was previously a manual and inconsistent workflow across differing prediction tasks and dataset formats. This reduces the likelihood of user error, improves the reproducibility of training and evaluation results across reports, and allows new prediction targets to be incorporated into the workflow without requiring separate custom pipelines for each one.

At present, the workflow is hosted in an internal LANL Git repository for version control and is not publicly available. We are actively working to generalize the workflow's prediction targets in and aim to make the workflow available in FY27 for others to use and apply to their datasets

4 Results and Discussion

Structural anomaly detection and prediction from vibration data using the ML workflow was evaluated in three independent sets of testing: one focused on coarse localization, another on simultaneous characterization of both stress and location, and a third test to look at fine-scale sensitivity to anomaly location. As a point of reference, training of the ML models used for the following predictions completed within several hours on a system equipped with an AMD EPYC Genoa 9334 CPU and an NVIDIA L40S GPU. While training rates varied from model to model, training was achieved within several dozens of epochs, each taking minutes to complete.

Testing for coarse defect localization consisted of deploying the mandrel in three configurations: absent/not inserted, inserted to a depth of 0 cm, and inserted to depth of 14 cm in the low-stress configuration. When the model was trained, validated, and tested on different windows cut from the same continuous time series, the mandrel configuration was correctly predicted 96% of the time. However, despite using randomized noise as the excitation course, this scenario does not represent a true independent test as the plug was not repositioned before re-collecting test data. When the model instead made inferences on an independent set of measurements collected after the mandrel had been reset and repositioned, the accuracy decreased slightly to 91.4% across all three configurations, with a maximum accuracy of 95.4% for an insertion depth of 14 cm (Figure 6). The overall accuracy represents an incorrect prediction rate for the model that is about 7.5 times lower than would be expected from a random guess. This indicates the chosen approach can achieve coarse localization with a high degree of accuracy using independent data, such as that would be collected as part of a real-time SHM system.

The success of the coarse-location test motivated the addition of stress level as a second independent variable for the model to simultaneously identify alongside stress location. Both variables of the experimental configuration were able to be correctly predicted in 81.3% of independently collected test samples (Figure Figure 7). Within these five tested configurations, the presence of the mandrel was correctly identified at an accuracy of 95%. Location was found to be easier to identify than stress, with very low levels of confusion between the two low-stress configurations, as well as the two high-stress configurations. The model performed better at distinguishing the stress level when the mandrel was positioned at a depth of 14 cm (average accuracy of 86%) as opposed to a depth of 0 cm (average accuracy of 70%). The reason for this

discrepancy between the two locations is not yet known and does not appear in the other tests, but likely reflects a minor repeatability issue when applying high levels of stress to the component via the mandrel.

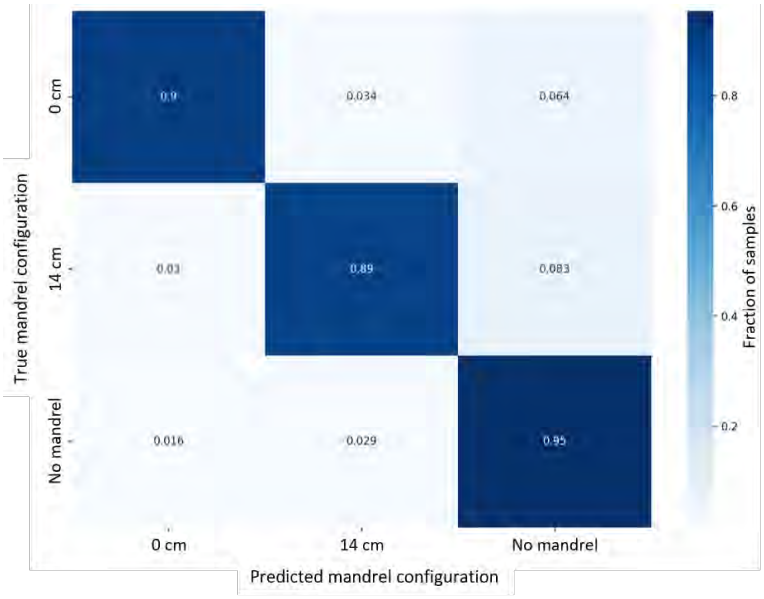


Figure 6. Predictions of the experimental configuration for an expanding mandrel in three configurations: absent, and inserted into the graphite block in a low-stress configuration at two locations (0 and 14 cm). Correct predictions in these confusions matrices fall along the diagonal.

Testing for fine-scale location sensitivity repeated the same general training, validation, and testing protocols as in the previously discussed tests but deployed the mandrel at 15 different locations in the low-stress configuration (inserted at one of 15 depths, from 0-14 cm in 1 cm steps). This resulted in collection of two independent 8 GB datasets for training/validation and testing uses.

For this fine-scale location prediction task, the model demonstrated reasonably strong performance when asked to identify the location of the mandrel within 1 cm (Figure 8): it identified the exact location of the stress anomaly in 27.5% of cases and was within ±1 cm of the correct location in 49.8% of cases across 15 possible categories. This represents a performance rate approximately 4 times better than random guessing, which would be expected to find the exact location only 6.7% of the time and be within ±1 cm just 19.1% of the time. We note a small bias in the model to incorrectly select the 14-cm location at a rate about twice that of other locations. This appears to be systematic behavior in the model to select the last item in its pre-defined list of prediction labels when there is a high degree of uncertainty in assigning a prediction label. We are actively investigating modifications to the internal parameters of the model to eliminate this bias and expect it to be resolved in the next 1-2 months.

Across all models, the window length used for training and prediction (5 ms) also represents the approximate time delay the model would need to make predictions on structural status from a real-time data feed in an operational setting. This short window length was chosen for benchtop

testing to maximize the number of training samples available from measurements of limited duration. However, real-time predictions are unlikely to require this rate, and operational data will not be similarly limited. Resonance-based SHM is most sensitive to progressive degradation in material or component properties—changes that typically emerge over hours, days, or years of operation—in contrast to techniques like acoustic emission, which are optimized to detect bursts of energy associated with local flaws rather than bulk degradation. When applied to real-time monitoring data streams, the technique presented here will not be data-limited. This greater data availability will enable longer window lengths, which in turn improve the spectral resolution used by the ML workflow, likely enhancing the fidelity and accuracy of the model's predictions.

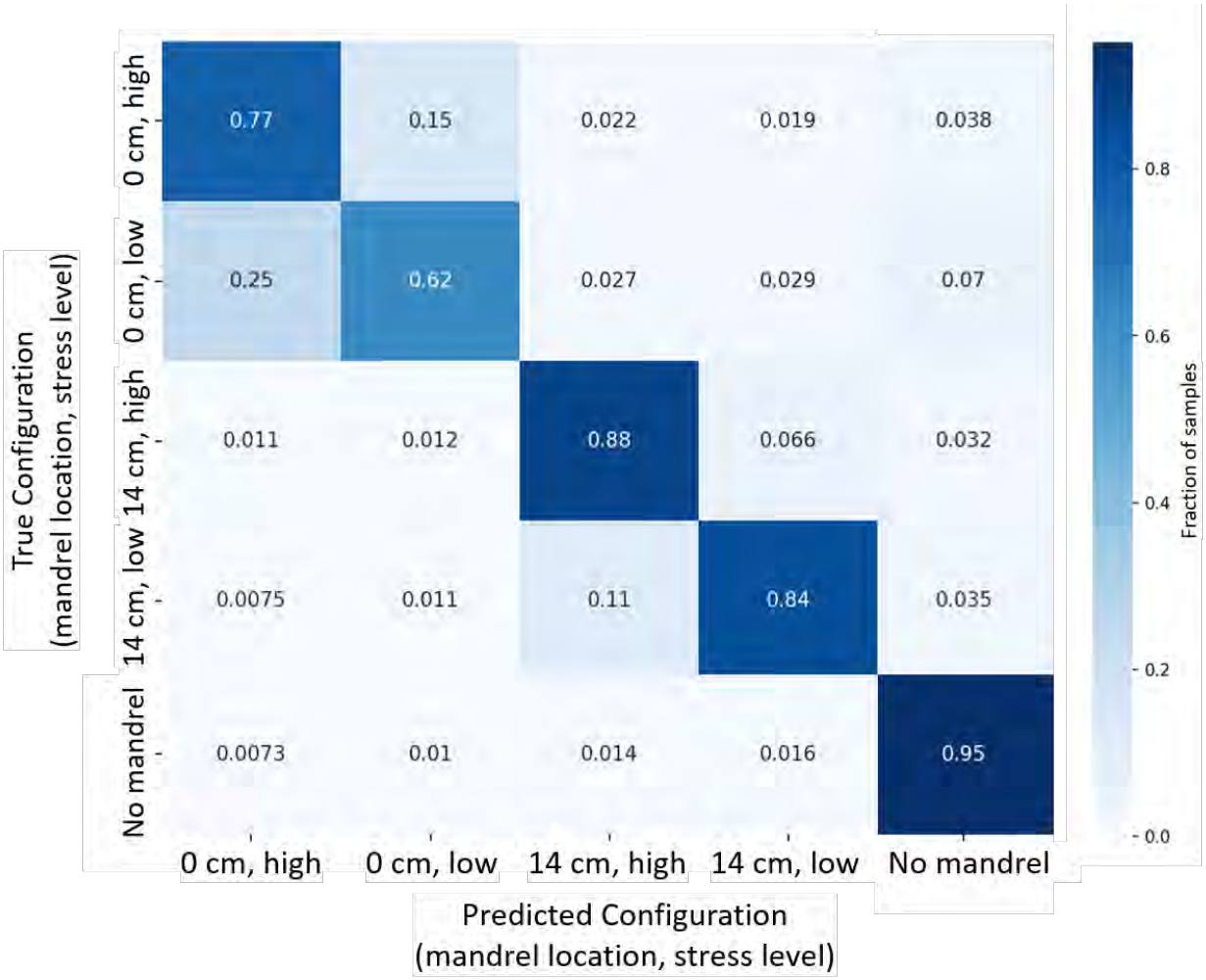


Figure 7. Predictions of the experimental configuration for an expanding mandrel in five configurations: absent, and inserted into the graphite block in a low-stress and high-stress configuration at two locations (0 and 14 cm).



Figure 8. Location predictions for an expanding mandrel inserted into the graphite block in a low-stress configuration at 15 depths, from 0 to 14 cm. Each column/row represents a 1-cm increment in the location of the inserted mandrel.

5 Conclusions and Future Work

Efforts in the second half of this fiscal year have focused on experimental development to further validate a machine learning-based approach for detecting and localizing structural anomalies in microreactor graphite components using ambient vibrational wavefield data. The project successfully established an experimental methodology involving insertable plug mechanisms, evolving from initial 3D-printed carbon-fiber designs with double-action expansion mechanisms to more refined approaches, to simulate structural stress conditions within a graphite test component. A user-friendly interface was developed to support both efficient model training and prediction workflows, with the explicit goal of minimizing manual tuning and enabling consistent use by non-specialist personnel. The predictive model itself showed promising technical performance for both coarse- and fine-scale localization of an artificial stress anomaly, achieving validation and prediction accuracies greater than 90%, even for data collected from un-seen measurements.

a validation accuracy of 92%. Work is currently underway to further build off these results, including greater generalization of the processing workflow to simultaneously handle predictions of multiple independent variables (e.g. mandrel depth and stress level). Training and validation success of the fine-scale localization is being used to bring the predictive workflow towards floating-point predictions, where it will soon be able to output more probabilistic predictions that are not restricted to a predefined list of classification labels.

In addition to work already in progress and being matured, priorities identified for continued progression in this area include:

- Adapting for true real-time monitoring – removing the barriers and delays associated with separately processing then predicting from a stream of input data.
- Confirmed-failure testing - extending validation to a component with a confirmed, realistic structural failure, incorporating multi-modal data representative of instrumentation found in actual microreactor control systems.
- Consideration of more realistic (variable) excitation and how that impacts model performance, and to what extent we can leverage ambient vibrations rather than active acoustic excitation

Collectively, these next steps aim to close the gap between promising algorithmic performance and field-ready structural health monitoring capability, moving this and related technologies closer to practical deployment in microreactor safety and monitoring systems.

6 References

[1] Arregui-Mena JD, Worth RN, Bodel W, März B, Li W, Campbell AA, et al. Multiscale characterization and comparison of historical and modern nuclear graphite grades. Mater Charact 2022;190. https://doi.org/10.1016/j.matchar.2022.112047.

[2] Zohuri B, McDaniel P. Advanced Smaller Modular Reactors: An Innovative Approach to Nuclear Power. Springer; 2019. https://doi.org/10.1007/978-3-030-23682-3.

[3] Marsden BJ, Haverty M, Bodel W, Hall GN, Jones AN, Mummery PM, et al. Dimensional change, irradiation creep and thermal/mechanical property changes in nuclear graphite. International Materials Reviews 2016;61:155–82. https://doi.org/10.1080/09506608.2015.1136460.

[4] Tanabe T. Radiation Damage of Graphite-Degradation of Material Parameters and Defect Structures. Phys Scr 1996;64:7–16.

[5] Anne A. Campbell, Brian D. Eckhart. Validation of the IMCE RFDA System for Dynamic Elastic Moduli Measurements 2015.

[6] Joyce MR, Marrow TJ, Mummery P, Marsden BJ. Observation of microstructure deformation and damage in nuclear graphite. Eng Fract Mech 2008;75:3633–45. https://doi.org/10.1016/j.engfracmech.2007.11.003.

[7] Liu D, Mingard K, Lord OT, Flewitt P. On the damage and fracture of nuclear graphite at multiple length-scales. Journal of Nuclear Materials 2017;493:246–54. https://doi.org/10.1016/j.jnucmat.2017.06.021.

[8] Moskovic R, Heard PJ, Flewitt PEJ, Wootton MR. Overview of strength, crack propagation and fracture of nuclear reactor moderator graphite. Nuclear Engineering and Design 2013;263:431–42. https://doi.org/10.1016/j.nucengdes.2013.05.011.

[9] Liu B, Zhao H, Li X, Yang Z, Zhang D, Liu Z. Effect of pore structure on the thermophysical and frictional properties of high-density graphite. Microporous and Mesoporous Materials 2022;330:111613. https://doi.org/10.1016/j.micromeso.2021.111613.

[10] Metcalfe M. Damage tolerance in the graphite cores of UK power reactors and implications for new build. Nuclear Engineering and Design 2023;406:112237. https://doi.org/10.1016/j.nucengdes.2023.112237.

[11] Bodel W, Martinuzzi P, Davies B, Steer A, Lowe T, Mummery P. Mimicking irradiation-induced cracking of nuclear graphite using bromine intercalation. Scr Mater 2021;199:10–3. https://doi.org/10.1016/j.scriptamat.2021.113889.

[12] Berg O, Eiler J, Garcia HE, Glöckler OS, Hashemian HM, Hines W, et al. On-line Monitoring for Improving Performance of Nuclear Power Plants, Part 2: Process and Component Condition Monitoring and Diagnostics. 2008.

[13] IAEA. Advanced surveillance, diagnostic and prognostic techniques in monitoring structures, systems and components in nuclear power plants 2013:139.

[14] Elshafey A, Marzouk H, Gu X, Haddara M, Morsy R. Use of fiber Bragg grating array and random decrement for damage detection in steel beam. Eng Struct 2016;106:348–54. https://doi.org/10.1016/j.engstruct.2015.10.046.

[15] Laffont G, Cotillard R, Roussel N, Desmarchelier R, Rougeault S. Temperature resistant fiber bragg gratings for on-line and structural health monitoring of the next-generation of nuclear reactors. Sensors (Switzerland) 2018;18. https://doi.org/10.3390/s18061791.

[16] Birri A, Sweeney DC, Hyer HC, Schreiber B, Cakmak E, Petrie CM. A Miniaturized, High-Bandwidth Optical Fiber Fabry-Perot Cavity Vibration Sensor Demonstrated up to 800 °C. IEEE Sensors 2025;25:11082–91. https://doi.org/10.1109/JSEN.2025.3541557.

[17] Daw JE, Good M, Meyer R, Ramuhalli P, Breon L. Assessment of Acoustic Sensor Application to Structural Health Monitoring of Reactor Components. 2022. https://doi.org/10.2172/2203075.

[18] Farrar CR, Dervilis N, Worden K. The Past, Present and Future of Structural Health Monitoring: An Overview of Three Ages. Strain 2025;61. https://doi.org/10.1111/str.12495.

[19] Farrar CR, Worden K. Structural health monitoring: a machine learning perspective. John Wiley & Sons; 2012.

[20] Xiao J, Cui F. Machine learning enhanced characterization of surface defects using ultrasonic Rayleigh waves. NDT and E International 2023;140:102969. https://doi.org/10.1016/j.ndteint.2023.102969.

[21] Lv G, Guo S, Chen D, Feng H, Zhang K, Liu Y, et al. Laser ultrasonics and machine learning for automatic defect detection in metallic components. NDT and E International 2023;133:102752. https://doi.org/10.1016/j.ndteint.2022.102752.

[22] Pyun D-K, Lee S, Palanisamy RP, Terricabras AJ, van Vuuren JJ, Jacobs D, et al. Comprehensive defect evaluation of advanced nuclear fuels using high-resolution acoustic signals and optimized sensor separation. NDT & E International 2026;157:103502. https://doi.org/10.1016/j.ndteint.2025.103502.

[23] Li Z, Kovachki N, Azizzadenesheli K, Liu B, Bhattacharya K, Stuart A, et al. Fourier Neural Operator for Parametric Partial Differential Equations. ICLR 2021 - 9th International Conference on Learning Representations 2021:1–16.

[24] Qin S, Lyu F, Peng W, Geng D, Wang J, Tang X, et al. Toward a Better Understanding of Fourier Neural Operators from a Spectral Perspective. CoRR 2024.

[25] Kaewnuratchadasorn C, Wang J, Kim CW. Neural operator for structural simulation and bridge health monitoring. Computer-Aided Civil and Infrastructure Engineering 2024;39:872–90. https://doi.org/10.1111/mice.13105.

[26] Geimer P, Delorey A, Bose R, Patelli A. Graphite Structural Assessment through Acoustic Resonance and Machine Learning. LA-UR-26-20537 2026.

[27] Sabharwall P, Hartvigsen JL, Morton TJ, Yoo J, Qin S, Song M, et al. Nonnuclear Experimental Capabilities to Support Design, Development, and Demonstration of Microreactors. Nucl Technol 2023;209:S41–59. https://doi.org/10.1080/00295450.2022.2043087.

[28] Trellue H, Taylor C, Luther E, Cutler T, Shivprasad A, Jewell JK, et al. Advancements in Yttrium Hydride Moderator Development. Nucl Technol 2023;209:S123–35. https://doi.org/10.1080/00295450.2022.2043088.

[29] Morton TJ, McKellar M, Sabharwall P, Jaison S. Development, Construction, and Operation of the Agile Non-nuclear Microreactor Experimental Test Bed (MAGNET) and Helium Component Test Facility (He-CTF). Nuclear Science and Engineering 2024;00:1–11. https://doi.org/10.1080/00295639.2024.2384218.

[30] General Atomics. Graphite design handbook. DOE-HTGR-88111 1988:1–122.

[31] Geimer PR, Delorey AA. Non-destructive structural characterization of graphite components using mechanical resonance and deep learning. LA-UR-25-29538 2025.